

## Chapter 1

### The Discovery of Helicity in Tilted Bent-Core Smectics: Sm(CP) <sub>$\alpha$</sub>

The discovery of spontaneous macroscopic polar ordering [?] and chirality [?] in fluid smectic liquid crystal phases of achiral bent-core mesogens has led to the exploration of a rich family of novel liquid crystal phases and self-assemblies [?, ?, ?, ?, ?, ?] in which the key macroscopic elements of polarity, chirality, and smectic layering all appear as spontaneously broken symmetries. While the smectic layer-scale order of bent-core mesogens, resulting from strong intralayer coupling between molecular tilt and polarity, is quite well characterized, superlayer structuring beyond that of the four basic SmCP bilayer phases combining synclinic or anticlinic tilt with ferroelectric or antiferroelectric polarity [?], as sketched in Supplemental Figure S1, have not been definitively identified. Possible superlayer structures analogous to those seen in tilted SmC\* phases of chiral, rod-shaped molecules could be incommensurate or commensurate with the underlying smectic layer spacing and feature states of varying azimuthal orientation of the molecular long axis about the layer normal,  $z$ , such as the chiral

put  
joe  
prc in  
begin-  
ning  
of sub-  
sec-  
tion

put  
biref/tilt  
figure  
in the  
optical  
textures/ele  
optics  
sec-  
tion

helical precession along  $z$  with equal, discrete orientational jumps between layers of the  $\text{SmC}_\alpha^*$  phase and the ferrielectric phases with periodic arrays of discrete jumps of different sizes [?].

Since the period of such superlayer structures,  $p$ , can be as short as two layers, the structural study of such phases requires the effective probing of molecular orientation at the nanoscale. This can be achieved using resonant X-ray scattering, a technique sensitive to atomic environment [?, ?, ?, ?, ?, ?, ?, ?, ?, ?, ?] that has previously enabled the discovery and definitive characterization of superlayer organization in several  $\text{SmC}^*$  phases and sub-phases, employing the K-edge resonance of atoms incorporated in the liquid crystal molecule [?, ?].

Several recent observations suggest the possibility of chiral superlayer ordering in achiral bent-core mesogens: Takanishi et al. have identified such a structure in a  $\text{SmCP}$  phase of a bent-core mesogen doped with a chiral, rod-shaped molecule that as a neat material exhibits  $\text{SmC}_\alpha^*$  and ferrielectric phases [?]; Abberley et al. have reported a superlayer helix in a smectic phase of bent dimers of molecular rods [?]; Panarin and co-workers have recently proposed, based on AFM evidence, the existence of tilted, helical supermolecular ordering in several achiral bent-core mesogens with 4-cyanoresorcinol bisbenzoate cores [?]. Earlier investigations of this molecular family had concluded, however, that their polar phases were orthogonal, i.e., untilted and therefore not chiral [?, ?]. Motivated by these conflicting reports and the ongoing interest in the chiral sub-phases of liquid crystals, we have studied one of the members of this homologous series, PAL30, which has  $n = 14$  alkyl tails (see Figure 1.1(a)). Our experiments, using non-resonant X-ray scattering (SAXS), resonant soft X-ray scattering (RSoXS), electro-optic techniques, and polarized light microscopy (PLM), summarized in Figure 1.1, reveal an exotic phase sequence, including an achiral de Vries smectic which becomes chiral in sufficiently large applied electric fields, and, at lower temperature, a tilted, chiral smectic with superlayer helical ordering.

## 1.1 Characterization of PAL30

We used a combination of two-dimensional, small-angle, hard X-ray scattering (SAXS), resonant, soft X-ray scattering (RSoXS), differential scanning calorimetry (DSC), polarized, transmitted light microscopy on cells in transmission, and measurements of the polarization reversal current of cells in order to characterize PAL30. These experiments reveal four smectic phases, labeled in order of descending temperature as Sm1, Sm2, Sm3, and Sm4.

### 1.1.1 Experimental Details

The RSoXS experiments were performed at the Advanced Light Source at Lawrence Berkeley National Laboratory beamline 11.0.1.2 using linearly polarized X-ray photons [?, ?]. The X-ray energy was tuned between 270 eV and 290 eV in our experiments, with scattering contrast appearing only for energies near the carbon K-edge resonance ( $E = 284$  eV), indicating the presence of real-space features with an orientational modulation. The PAL30 material was sandwiched between two silicon nitride substrates, while in the isotropic phase. The cell was then placed into a temperature controlled hotstage in the beamline. After finding the highest temperature where scattering features were observed, the sample was cooled slowly while recording 2D diffractograms of the scattering. The RSoXS setup is sensitive to orientational modulations from  $d = 50$  Å to 1250 Å. The relative positions and orientations of the sample and detector were calibrated using a sample with known scattering  $q$ -values. The data from the detector was processed using the Igor Pro-based NIKA data reduction software package [?, ?].

The angular resolution of the diffractometer, estimated from the full width at half-maximum of a resonant feature known to be twice the smectic layer spacing is  $\delta q \sim 0.00078$  Å<sup>-1</sup>.

SAXS measurements were carried out on beamline X10A of the National Synchrotron Light Source (NSLS), at Brookhaven National Laboratory. This beamline has a Si 111 double

monochromator, tuned to around 10 keV. The sample was mounted in an Instec hot stage on a Huber four-circle goniometer. The angular resolution of the diffractometer, measured by scanning the detector arm through the attenuated direct beam, is  $\delta q \sim 0.005 \text{ nm}^{-1}$  full width at half-maximum.

The planar cells used for texture analysis were 4.5  $\mu\text{m}$  thick commercial cells purchased from Instec Inc. with rubbed polyimide planar alignment layers and ITO glass. The thickness of the empty cells was measured using a visible light spectrometer. The cells were then filled with PAL30 in the isotropic phase. Polarization reversal current was measured in these cells by applying an alternating, triangular voltage.

The birefringence was measured using a Zeiss quartz-wedge compensator and a 5.86  $\mu\text{m}$  thick Instec cell.

The molecular length of PAL30 was estimated using a Hartree-Fock 6-31G\* calculation of a single molecule in the gas phase using the Spartan  $\ddot{\text{A}}\ddot{\text{Y}}16$  numerical calculation package.

### 1.1.2 Differential Scanning Calorimetry of PAL30

The DSC reveals only a single enthalpy peak on cooling, at approximately 110 °C, hinting that the Sm1  $\rightarrow$  Sm2 transition is either a weakly first order, or a second order transition.

The lack of other enthalpy peaks is concerning, considering we identify four unique smectic phases in the phase sequence of PAL30. However, the resonant scattering experiments described in [subsection 1.1.3](#), particularly the soft-melting mode seen in [Figures 1.4](#), shows that the phase transition from the Sm2  $\rightarrow$  Sm3 is strongly second order, spanning a temperature range of 10 °C, which explains the absence of a distinct enthalpy peak in the DSC for this transition.

The lack of a distinct peak for the Sm3  $\rightarrow$  Sm4 peak has two plausible explanations. First, the polarization current shown in ?? shows that the transition is likely second order,

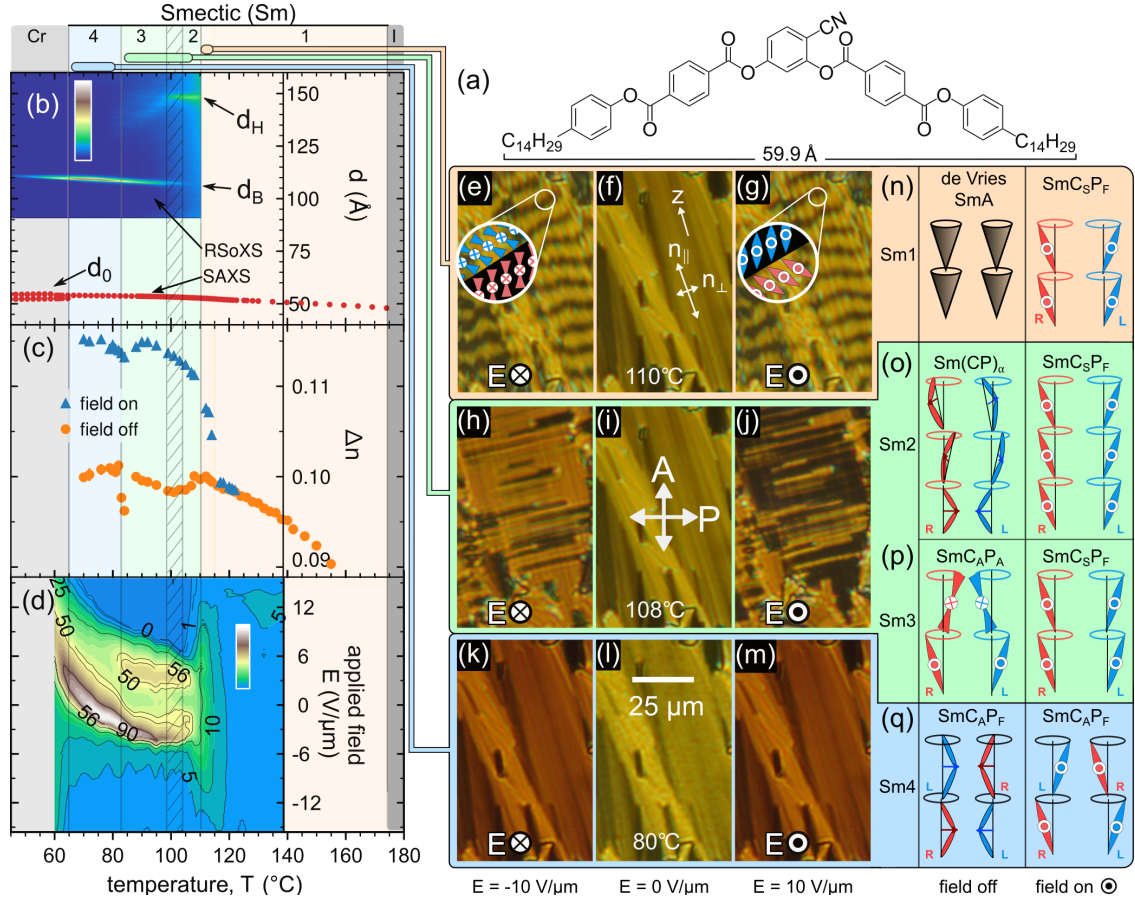


Figure 1.1: Experimental characterization of PAL30. (a) The PAL30 molecule, showing the all-trans length calculated using the program Spartan. (b–d) Phase properties vs. temperature. The solid vertical lines denote phase boundaries and the cross-hatching phase coexistence. (b) SAXS shows the smectic layer spacing in all phases to be  $d_0 \approx 48 \text{ \AA}$ . Resonant carbon K-edge reflections are from superlayer modulations of the molecular orientation about the layer normal  $z$ , the peak at  $d_H \approx 150 \text{ \AA}$  corresponding to the pitch of the incommensurate, helical precession in the Sm2 phase, and at  $d_B = 2d_0$  to the bilayer ordering of the Sm3 and Sm4 phases. (c) Birefringence of planar-aligned cells with layers normal to the plates, with and without applied electric field ( $E = 20 \text{ V}/\mu\text{m}$ ). (d) Polarization current (in nA) in response to a triangle-wave applied electric field: a single-peak, Langevin-like response at lower temperatures in the Sm1 phase; a triple peak in the Sm2 phase, associated with ferrielectric switching[?] and indicative of helical unwinding[?], coalescing into a double peak in the Sm3, indicating a non-polar ground state at  $E = 0$ ; and a single current peak in the Sm4 phase caused by the block polarization switching of the ferroelectric Sm<sub>C\_A</sub>P<sub>F</sub> ground state. (e–m) Characteristic optical textures in a planar cell, viewed between crossed polarizers. The  $E = 0$  textures are focal conics typical of a fluid smectic with an optic axis along  $z$ . Field application induces chiral, tilted conglomerate domains (of opposite handedness) in the Sm1–Sm3 phases, but only a change in birefringence in the Sm4. (n–q) Proposed superlayer structure of PAL30 phases, with and without applied electric field: (n) Sm1: achiral de Vries-like SmA → chiral Sm<sub>S</sub>P<sub>F</sub>; Sm2: superlayer chiral helix → chiral Sm<sub>S</sub>P<sub>F</sub>; Sm3: superlayer chiral bilayer Sm<sub>C\_A</sub>P<sub>A</sub> → chiral Sm<sub>S</sub>P<sub>F</sub>; Sm4: Sm<sub>C\_A</sub>P<sub>F</sub> with **P** parallel to the glass → Sm<sub>C\_A</sub>P<sub>F</sub> with **P** normal to the glass.

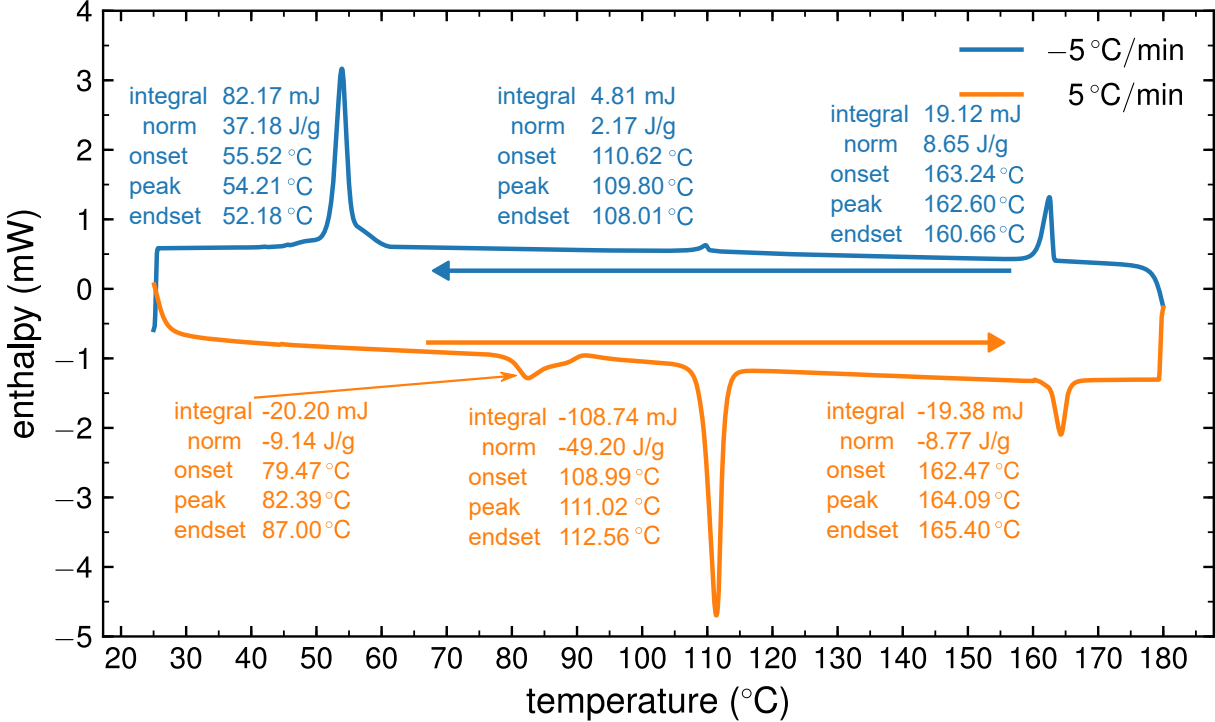


Figure 1.2: Differential scanning calorimetry of PAL30. On cooling, there is only a small, enthalpy peak at  $\approx 110^\circ\text{C}$  corresponding to the transition from the highest-temperature smectic phase, the Sm1, and the Sm2.

spanning a temperature range of approximately  $5^\circ\text{C}$ , like the  $\text{Sm}2 \rightarrow \text{Sm}3$ . Though, as the identified structures of the  $\text{Sm}3$  ( $\text{SmC}_\text{A}P_\text{A}$ ) and  $\text{Sm}4$  ( $\text{SmC}_\text{A}P_\text{F}$ ) cannot be connected by a continuous deformation the same way the helical  $\text{Sm}2$  ( $\text{Sm}(\text{CP})_\alpha$ ) can be deformed into the  $\text{Sm}2$  ( $\text{SmC}_\text{A}P_\text{A}$ ), this seems less likely.

The other explanation, which I consider more likely, is due to the fact the DSC is measured without a field present, raising the possibility first explored by Guzman[?] for orthogonal phases, that the transition from the  $\text{SmC}_\text{A}P_\text{A}$  to the  $\text{SmC}_\text{A}P_\text{F}$  could be a kinetic trap. If this was the case, then the  $\text{SmC}_\text{A}P_\text{A}$  would be expected to be the ground-state phase *in absence of an applied field* for the remainder of the phase sequence. This could be tested in future experiments with the DC hysteresis measurements described in Dr. Guzman's thesis[?].

### 1.1.3 X-ray Scattering of PAL30

X-ray scattering from PAL30 is shown in Figures 1.1(b) and S3.

Upon cooling from the isotropic, a single, non-resonant SAXS peak appears at 175 °C, at a wavevector  $q_0$  corresponding to Bragg scattering from the smectic layers in the Sm1 phase with spacing  $d_0 = 2\pi/q_0 = 48 \text{ \AA}$ .

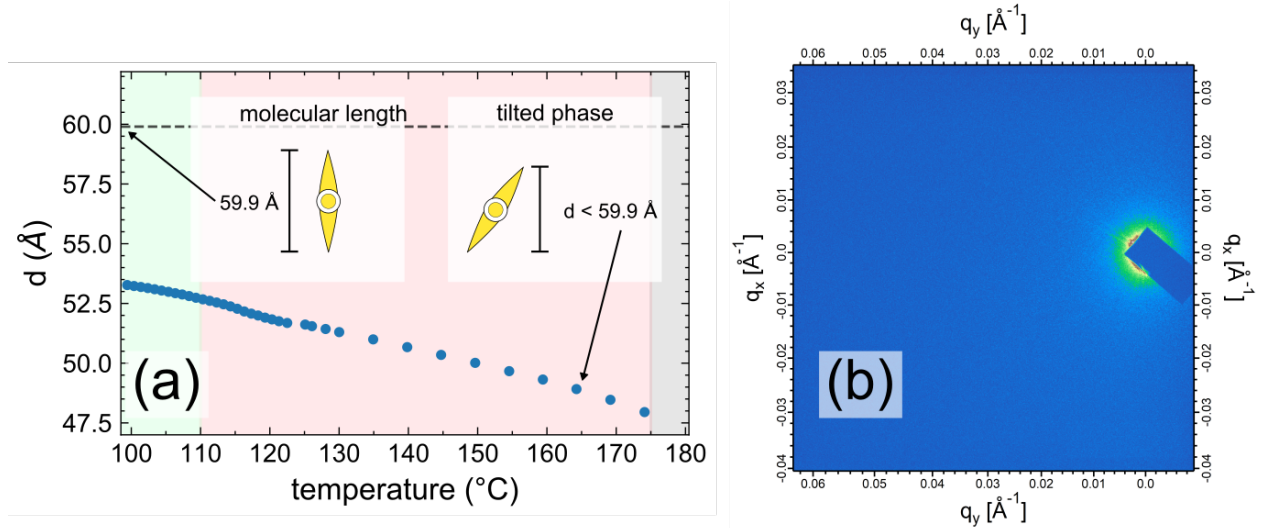


Figure 1.3: X-ray scattering of high temperature phase, Sm1, of  $\text{Sm}(\text{CP})_\alpha$ . (a) The smectic layer size,  $d$ , increases monotonically on cooling, with no inflection points that would be characteristic of a untilted→tilted phase transition. (b) No resonant scattering is observed for this phase.

The layer spacing increases slightly on cooling to the crystal phase at 65 °C and is consistently smaller than the calculated molecular length,  $l = 59.9 \text{ \AA}$ , throughout this temperature range, suggesting that the molecules are tilted in all of the smectic phases, to first order by an average amount estimated using  $\theta_{\text{xray}} = \cos(d_0/l)$  of 33° (see Figure S4). In the Sm1 temperature range ( $110^\circ\text{C} \leq T \leq 175^\circ\text{C}$ ), there are no RSoXS scattering features (Figure 1.3 (b)) that would indicate a superlayer periodic structure.

At the transition to the Sm2 phase, at 110 °C, marked by a distinct enthalpy peak in the DSC (Figure S5), a single, sharp resonant peak appears at  $q_H = 0.042 \text{ \AA}^{-1}$ , corresponding to

a molecular orientational structure with a period  $d_H = 148 \text{ \AA} \approx 2.8d_0$  that is incommensurate with the smectic layer spacing (Figure 1.5(b) and Figure 1.4). Below 104 °C, this reflection becomes weaker and another sharp, resonant reflection at higher  $q$  grows in, the coexistence indicating a first-order transition to the Sm3 phase. This second Bragg peak, which persists down to the crystal phase, has a wavevector  $q_B \approx q_0/2$ , indicative of a commensurate, bilayer orientational structure in the Sm3 and Sm4 phases.

Below 99 °C, the incommensurate peak broadens dramatically and moves to higher  $q$ , indicating the presence of short-ranged, Sm2-like helical fluctuations persisting in the Sm3 phase, and disappears at the transition to the Sm4 phase at 83 °C. The Sm4 phase exhibits only the bilayer RSoXS reflection at  $q_B$ .

The RSoXS scattering from a single layer can be analyzed, following Levelut and Pansu, in terms of a monoclinic second-rank tensor with a principal axis tilted from and then azimuthally rotated about the layer normal [?, ?, ?]. Scattering from a stack of such layers is calculated by summing over the contributions of the individual layers at different  $z$ . Resonant scattering peaks from azimuthally periodic arrangements are found at wavevectors along  $z$ ,  $q(l, m) = l(2\pi/d_0) \pm m(2\pi/p)$ , where  $p$  is the pitch. In principle, resonant scattering should appear at all values of  $l$  (harmonics of  $q_0$ ), and at values of  $m = 0, \pm 1, \pm 2$  that depend on the superlayer structure. In an incommensurate, helical structure, like the SmC $\alpha$  phase, only the fundamental and harmonic peaks at  $q(l = 0, m = +1, +2)$  and the Umklapp peaks at  $q(l = +1, m = -1, -2)$  are found in the range  $0 < q(l, m) < q_0$ . If the resonant scatterers are confined to lie precisely on layers spaced by  $d_0$ , then the intensities of these peaks will be identical [?]. Out-of-layer molecular positional fluctuations, and, in particular, those for which there is a coupled azimuthal orientation that keeps the molecule on the helix,  $\delta\phi = (2\pi/p)\delta z$ , reduce the intensities of the resonant harmonic peak at  $2q_H$  and of the Umklapp peaks at  $q_0 \pm q_H$ , relative to that of the fundamental at  $q_H$  [?]. In our RSoXS scans of these peaks, only the fundamental is seen above the background, so that only the upper limit of the intensity ratio of the Umklapp and fundamental peaks can be estimated.

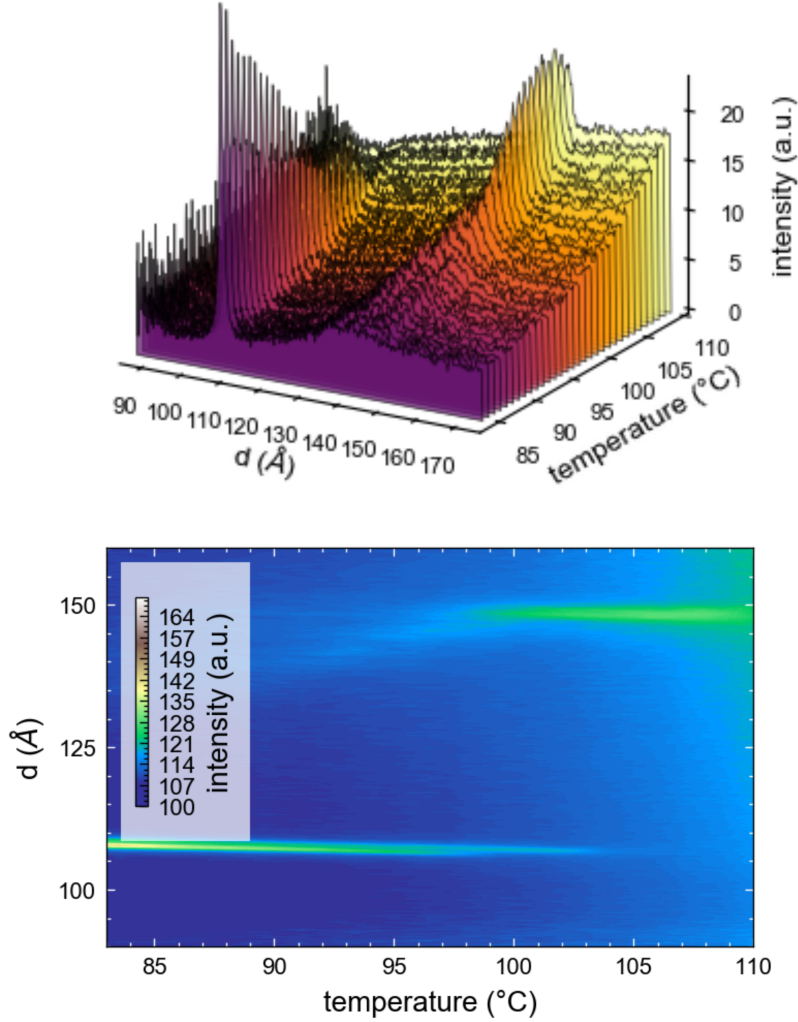


Figure 1.4: Temperature behaviour of the  $\text{Sm}(\text{CP})_\alpha$  phase plotted as a waterfall plot in (a), and as a contour plot in (b). A bilayer ( $d = 112 \text{ \AA} = 2d_0$ ) corresponds to the 2-layer unit-cell structure of the  $\text{SmCPA}$  phase, which sits directly below the  $\text{Sm}(\text{CP})_\alpha$  phase in temperature. The resonant peak corresponding to the  $\text{Sm}(\text{CP})_\alpha$  phase at  $d \approx 150 \text{ \AA}$  is direct evidence that the  $\text{Sm}(\text{CP})_\alpha$  phase is not a classic B2-type phase.

From the RSoXS heating scan of Figure 1.5(a), we find  $I_U/I_F \lesssim 0.03$ , implying a very weak fractional modulation of the density of helical scatterers,  $\rho$ , due to fluctuations in the smectic layering  $\sqrt{\langle \delta\rho^2 \rangle}/\rho_0 < 0.17$ . The absence of the harmonic peaks places a similar limit on how much the density modulation of helical scatterers deviates from being purely sinusoidal.

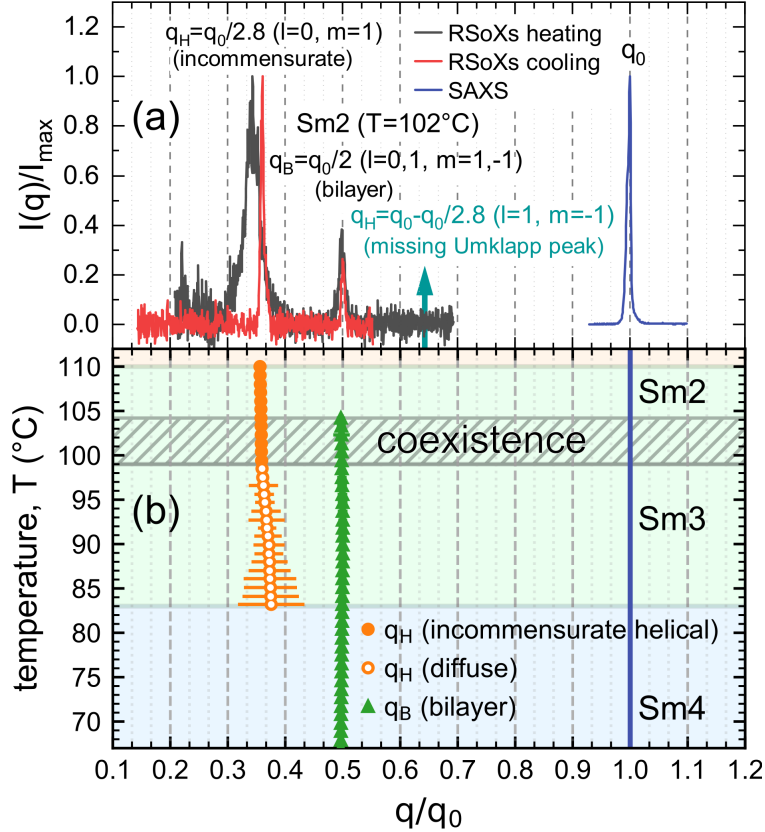


Figure 1.5: X-ray scattering from PAL30. (a) SAXS gives a peak from the smectic layer ordering at  $q = q_0$ . The RSoXS peak at  $q_H$  indicates that there is superlayer orientational ordering with periodicity  $d_H$  in the Sm2 phase. In general, superlayer orientational modulation in a smectic generates RSoXS peaks at wavevectors along the layer normal at  $q(l, m) = l(2\pi/d_0) \pm m(2\pi/d_H)$ [?]. The observation of an RSoXS reflection at  $q = q(0, 1)$  and the absence of an Umklapp peak at  $q = q(1, -1)$  in the Sm2 confirms a superlayer helix with a scattering amplitude modulation due to the smectic layering that is undetectably weak. (b) Temperature dependence of resonant scattering. The helix peak at  $q_H \approx 1/(2.8d_0)$  becomes diffuse in the Sm3 phase. Splitting of the bilayer peak at  $q_B$ , which would indicate helical precession of the bilayer structure, is not observed.

### 1.1.4 Optical Textures

The optical textures of planar-aligned (bookshelf) cells of PAL30 were studied using PLM. Upon cooling from the isotropic, the Sm1 phase grows in (at 175 °C) as bâtonnets, giving a smooth, focal-conic texture typical of an orthogonal fluid smectic (Figure 1.1(f), Figure 1.6).

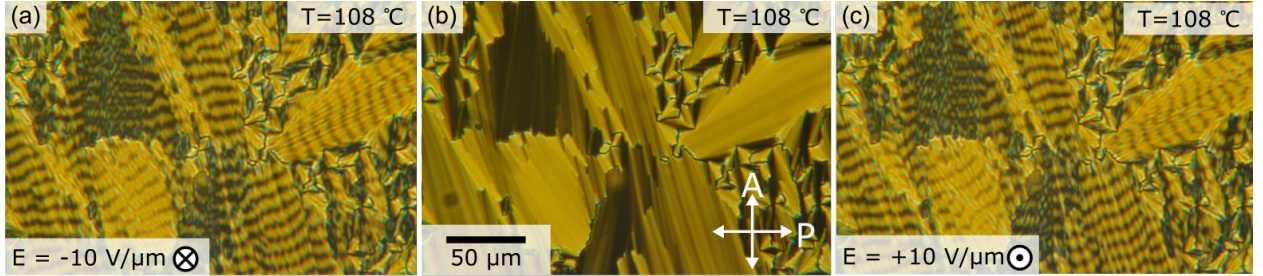


Figure 1.6: Planar aligned textures of Sm1. (a) Applied field out of the page, (b) ground state (no field), (c) applied field into the page.

However, given the large value of the estimated molecular tilt,  $\theta_{\text{xray}}$ , the Sm1 is probably a de Vries smectic. In planar-aligned cells, there is no observable field-induced change of the in-plane birefringence,  $\Delta n = n_{\parallel} - n_{\perp}$ , in small applied electric fields (Figure 1.1(f)), or in the optic axis orientation,  $\theta_{\text{opt}}$  (Figure 1.7).

Below 115 °C, a threshold field,  $E_{\text{th}}$ , above which a first-order structural change marked by the appearance of chiral conglomerate domains occurs, becomes experimentally accessible. These domains are polar and exhibit a uniform, saturated optic axis tilt on the order of  $\theta_{\text{opt}} \approx 18^\circ$  from the layer normal, implying that the achiral, untilted Sm1 phase transforms in the field to a B2-like, homochiral  $\text{SmC}_S P_F$  state (Figure S1(c)) [?]. The field-induced left- and right-handed domains form a “tiger stripe” pattern (Figures 1.1(e,g)).

The local domain handedness in this unusual conglomerate texture is apparently locked in after the first few field cycles. This bias is due to a chiral memory effect at the surface since, as Figures 1.1(d) and 1.7 show, the sub-threshold bulk state has an achiral field response, with

a linear polarization current (implying  $P \propto E$ ) and no detectable reorientation of the optical tilt.  $E_{\text{th}}$  decreases strongly on cooling as the transition to the Sm2 phase is approached, as shown in the inset of Figure 1.7.

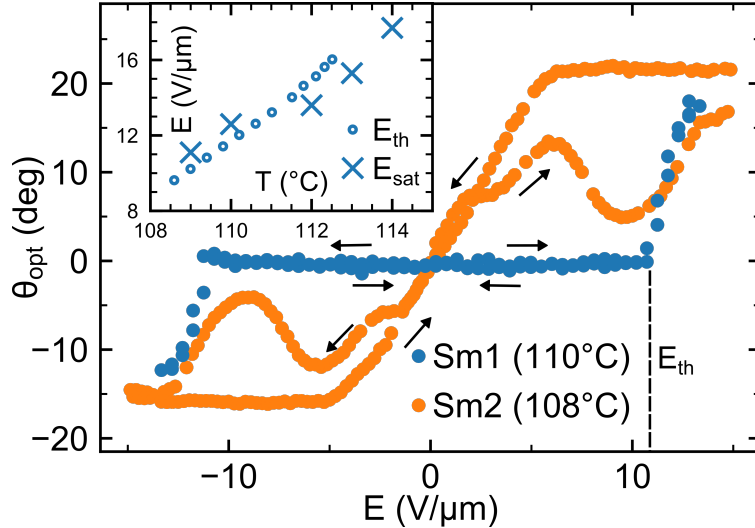


Figure 1.7: Optical tilt of PAL30 vs. applied field. The Sm1 phase shows no electrooptic response in weak fields  $E < E_{\text{th}}$ . Fields  $E > E_{\text{th}}$  induce an electroclinic tilt and result in the formation of chiral domains.  $E_{\text{th}}$ , which becomes smaller with decreasing  $T$  (inset), matches closely  $E_{\text{sat}}$ , the field at which the induced polarization saturates, extracted from Figure 1.1(d). The Sm2 phase exhibits a chiral electroclinic effect near  $E = 0$  and hysteresis in the field-induced helix unwinding to the  $\text{SmC}_\text{S}P_\text{F}$  state.

In the lower part of the Sm1, and throughout the Sm2, Sm3 and Sm4 phases, the birefringence increases on application of an electric field, as seen in Figure 1.1(c), changing from yellow to orange. Measurements of  $\Delta n$  at  $E = 0$  and  $E = 20 \text{ V}/\mu\text{m}$  (Figures 1.1(c) and S6), show that the birefringences in the lower temperature phases with and without an applied field are of the order of  $\Delta n_{\text{on}} \sim 0.12$  and  $\Delta n_{\text{off}} \sim 0.10$ . Assuming that the field-on  $\text{SmC}_\text{S}P_\text{F}$  state (Figures 1.1(n–p) and S1) gives a uniform director orientation with the optic axis in the plane of the cell, then  $\Delta n \sim 0.12$  would correspond to the maximal birefringence  $n_3 - n_1$  of the  $\text{SmC}_\text{S}P_\text{F}$  state. Modeling the bent-core molecule as two uniaxial, birefringent rods connected with an opening angle of  $\Psi$ , and tilting this molecule from  $z$  by an angle  $\theta$ , we have calculated the birefringence of all of the states shown in Figure 1.1. If the Sm1 phase

is assumed to be a de Vries SmA, with azimuthally averaged molecules distributed on a tilt cone of angle  $\theta$ , the best fit to the measured birefringence values  $\Delta n_{\text{on}}$  and  $\Delta n_{\text{off}}$  is obtained with  $\Psi = 150^\circ$  and  $\theta = 15^\circ$ . The calculated birefringence as a function of temperature is shown in Figure S6.

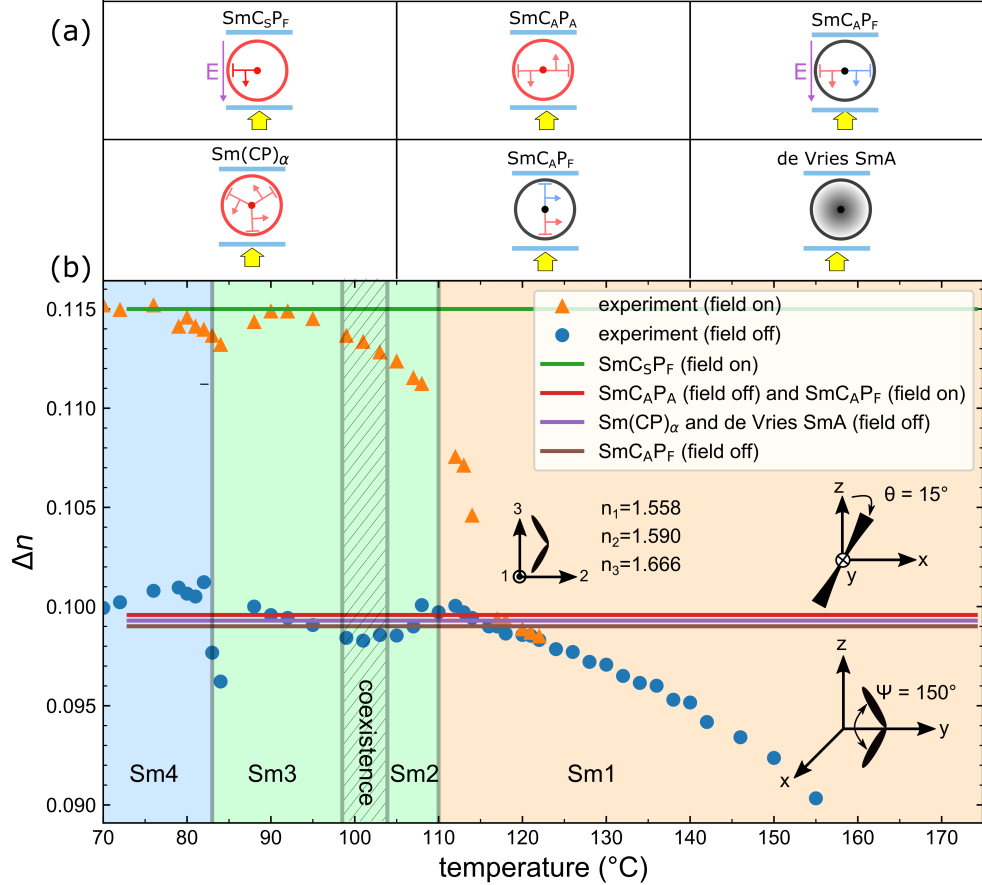


Figure 1.8: Calculated birefringence of PAL30, assuming Boulder phase assignments, shown as a function of temperature

The transitions between the smectic phases are difficult to see when  $E = 0$  because they are all orthogonal in appearance, with an optic axis along  $z$ , and have similar birefringence. At the transition from Sm1 to the Sm2 phase, however, arbitrarily small electric fields induce molecular tilt in the (Figure 1.7), leading to the formation of optically distinct, conglomerate chiral domains with opposite tilt (Figures 1.1(h–j)), again corresponding to a field-induced transition to a *SmCP<sub>F</sub>* state. The birefringence and orthogonal appearance of the Sm2

ground state are consistent with the helical superlayer structure indicated by RSoXS.

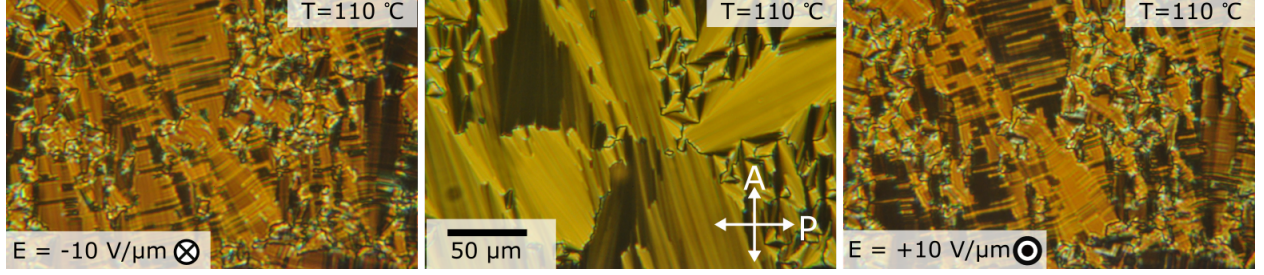


Figure 1.9: Textures of both the Sm2 ( $\text{Sm}(\text{CP})_\alpha$ ) and Sm3 ( $\text{SmC}_\text{A}\text{P}_\text{A}$ ) phases of PAL30: reminiscent of a  $\text{SmC}_\text{A}\text{P}_\text{A}$  texture.

The texture and birefringence of the Sm3 phase in the absence of field are consistent with the  $\text{SmC}_\text{A}\text{P}_\text{A}$  bilayer structure indicated by RSoXS. The field-induced conglomerate domain morphology in both the Sm2 and Sm3 phases is distinct from that of the undulating Sm1 tiger stripes, with straight domain boundaries that tend to form parallel to the layers, as in an antiferroelectric calamitic being driven to a ferroelectric state [?]. The optical tilt in these domains is found to be  $\theta_{\text{opt}} \sim 18^\circ$ .

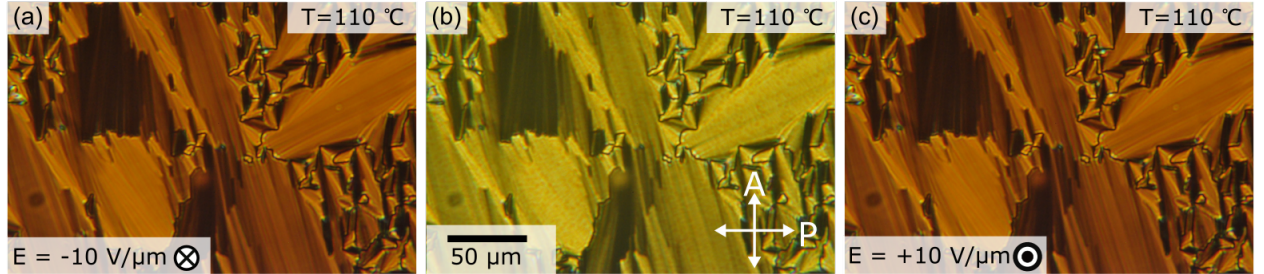


Figure 1.10: Textures of both the Sm2 ( $\text{Sm}(\text{CP})_\alpha$ ) and Sm3 ( $\text{SmC}_\text{A}\text{P}_\text{A}$ ) phases of PAL30: reminiscent of a  $\text{SmC}_\text{A}\text{P}_\text{A}$  texture.

The response to applied field changes dramatically again at the transition from Sm3 to Sm4, with no visible brush rotation or evidence of domain formation at any  $E$ .

The birefringence in the Sm4 phase increases continuously with field, saturating at a value comparable to that observed in the field-induced Sm2 and Sm3 conglomerate domains.

### 1.1.5 Polarization Current

The polarization current, measured with a triangular applied field, for the entire phase sequence is shown vs. temperature in Figures 1.1(d) [Figure 1.11](#). The polarization current will be discussed in order of cooling.

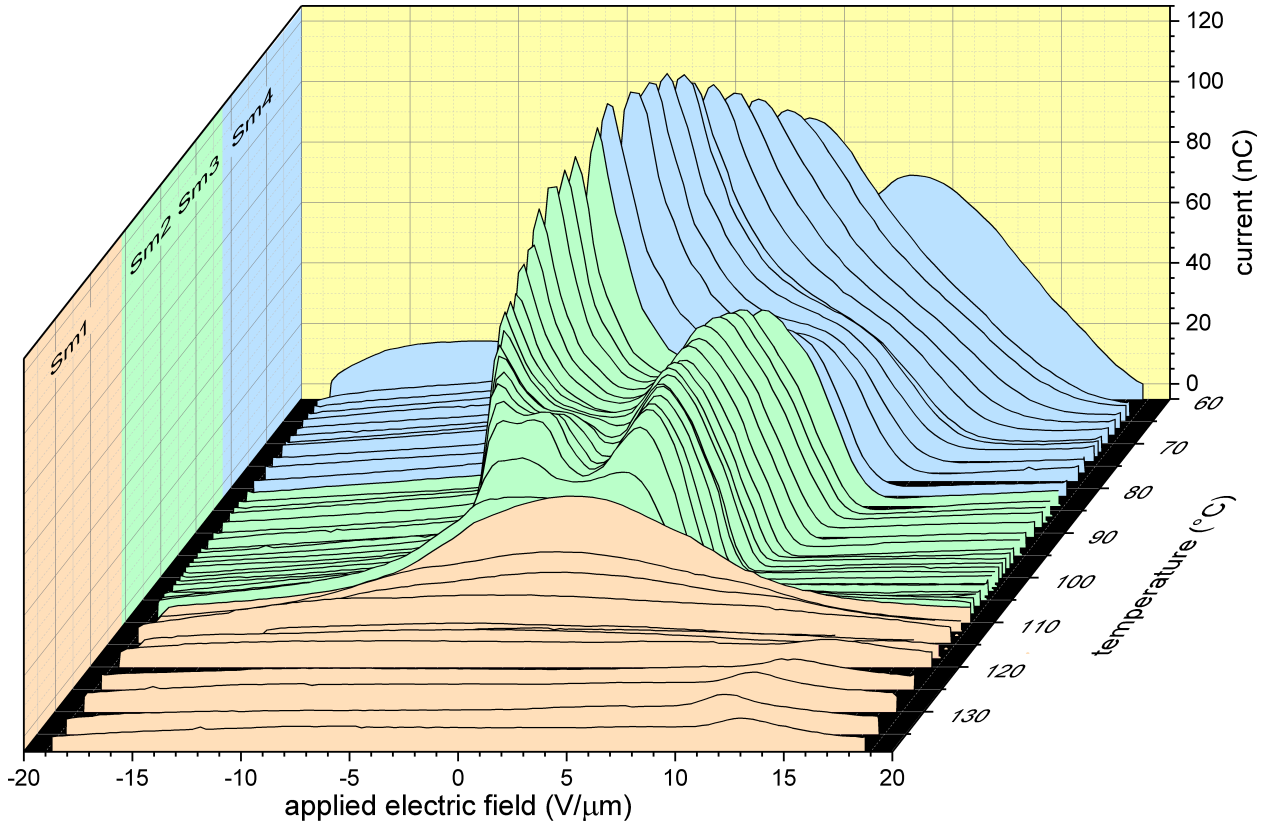


Figure 1.11: Polarization current of PAL30 shown as a function of the applied field strength.

Upon cooling from the isotropic, a single current bump centered about  $E = 0$  first appears at lower temperatures in the Sm1 phase, indicating a Langevin-type field-induced orientation of  $\mathbf{P}$ , with a linear response near  $E = 0$  and the current vanishing when  $\mathbf{P}$  becomes saturated (for  $E \geq E_{\text{sat}}$ ).

Significantly,  $E_{\text{sat}}$  is similar in magnitude to  $E_{\text{th}}$ , the threshold field required for the Sm1 transition to chirality observed optically ([Figure 1.7](#), inset), indicating that the field first orders the Langevin system of initially azimuthally random molecular polarizations, with the

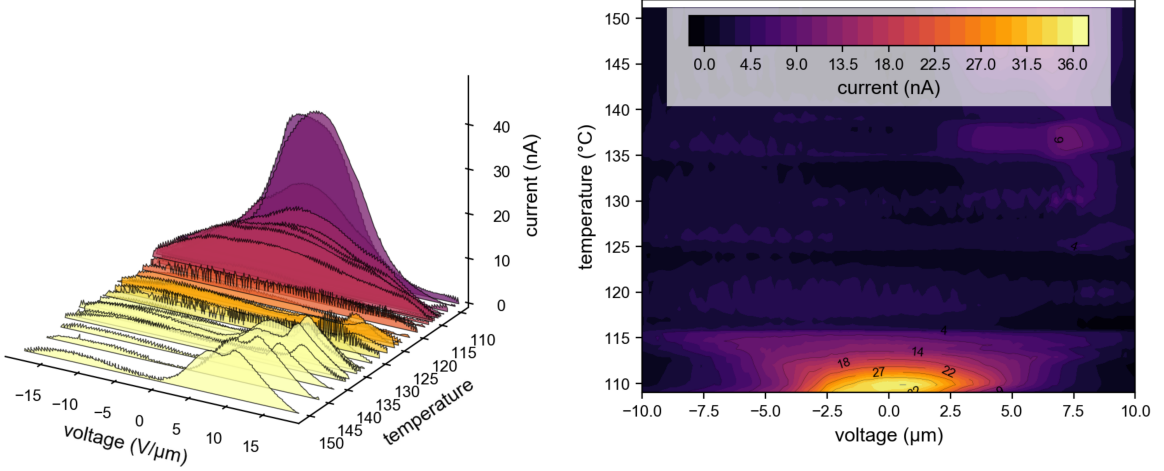


Figure 1.12: Zoomed in polarization current measurements for PAL30 in the high temperature Sm1 phase.

Sm1 remaining in an achiral state, and that the phase becomes chiral only at higher fields, once  $\mathbf{P}$  is saturated (Figure S10).

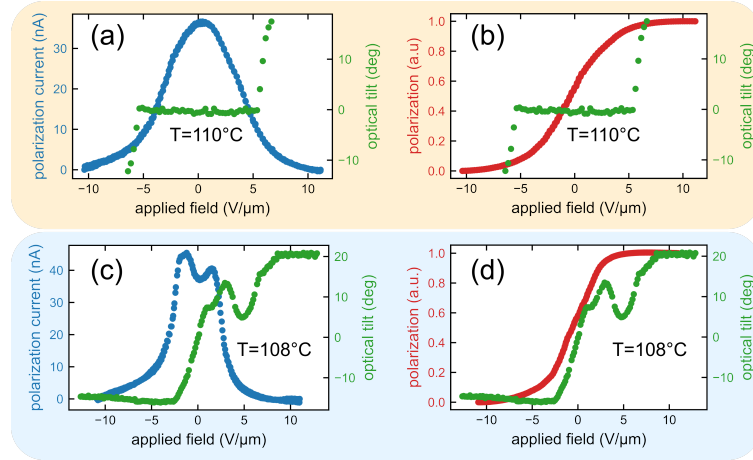


Figure 1.13: The polarization current and the optical tilt plotted as a function of applied field strength for both the Sm1 (de Vries SmA) (a,b) and the Sm2 ( $\text{Sm}(\text{CP})_\alpha$ ) (c-d). The polarization current has additionally been integrated to calculate the time-dependant net polarization. The threshold electric field ( $E_{\text{th}}$ ) required to manifest the tiger-stripes can be directly read from the green curve denoting the optical tilt (for  $T=110^\circ\text{C}$ ,  $E_{\text{th}} \approx 5 \text{ V}/\mu\text{m}$ ), and the saturation electric field where the net polarization is no longer changing ( $E_{\text{sat}}$ ) can be directly read from the red curve, which denotes the net polarization, (for  $T=110^\circ\text{C}$ ,  $E_{\text{sat}} \approx 5 \text{ V}/\mu\text{m}$ ). Both  $E_{\text{th}}$  and  $E_{\text{sat}}$  are plotted in as the inset of Figure 1.7.

On cooling to the Sm2 phase, the polarization bump splits into three peaks roughly centered about  $E = 0$  that evolve to two peaks on cooling through the Sm3, shown in Figure 1.14.

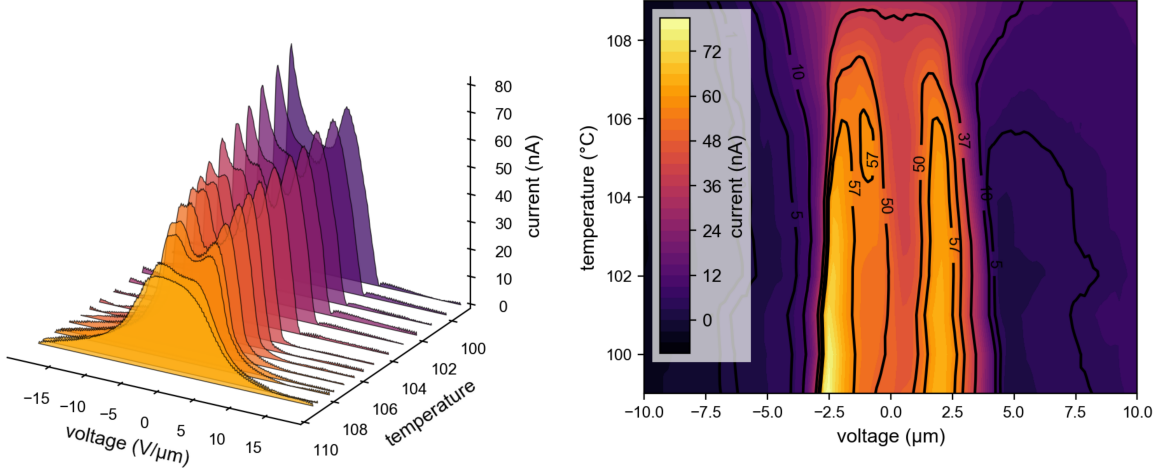


Figure 1.14: Polarization current of sm2 of PAL30 plotted against applied voltage

PAL30 thus transforms on cooling from the non-polar Langevin ground state of the Sm1, where  $P = 0$  is enforced by entropy, to energetically stabilized ground states in which the spatial average of  $\mathbf{P}(\mathbf{r})$  in the absence of applied field is also zero: the incommensurate helical winding of the polarization in the Sm2, and the antiferroelectric bilayer structure in the Sm3.

At the transition to the Sm4, a single current peak dominates, characteristic of the block polarization switching of a ferroelectric ground state that is surface-stabilized with  $\mathbf{P}$  parallel to the cell plates at  $E = 0$ , such as occurs in the orthorhombic  $\text{SmAP}_\text{F}$  phase [?].

The absence of brush rotation during the field-induced reorientation of the polarization in Sm4 is consistent with achiral  $\text{SmC}_\text{A}\text{P}_\text{F}$  superlayer organization.

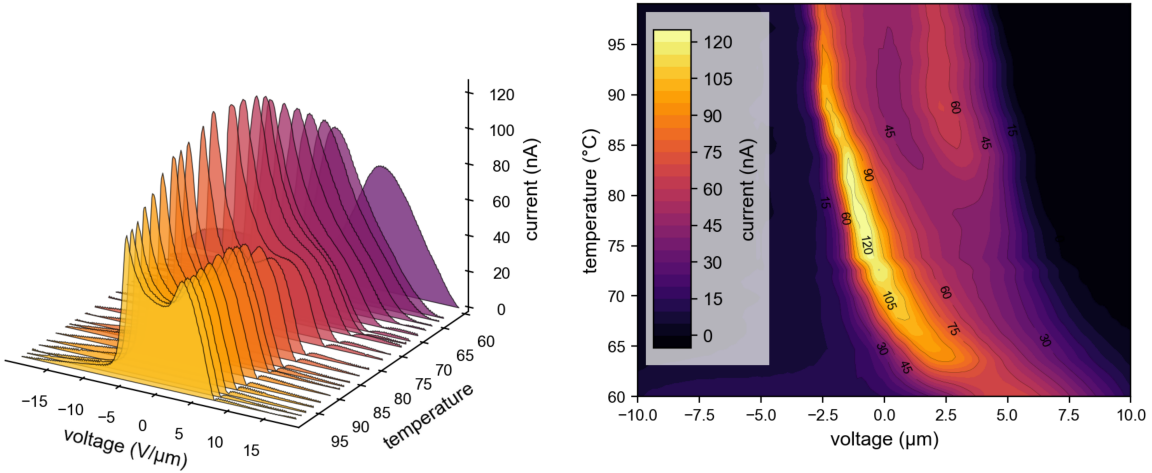
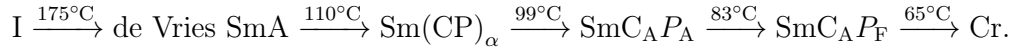


Figure 1.15: Polarization current measurements for PAL30 in the high temperature Sm1 phase.

## 1.2 Results and Discussion

In summary, X-ray and optical experiments show that PAL30, an achiral, bent-core mesogen, forms smectic liquid crystal phases with the molecules substantially tilted from the layer normal, with phase sequence:



The highest temperature phase exhibits short-ranged ordering of the tilt azimuth that is decoupled from the molecular polarization, forming a uniaxial, non-polar, achiral de Vries smectic A. An applied electric field of increasing magnitude continuously aligns the initially random polarization and the phase acquires orthorhombic symmetry. The field eventually saturates the polarization orientation, inducing a transition to a tilted, chiral, ferroelectric smectic state.

Upon cooling, a novel chiral, ferrielectric phase which we call the  $\text{Sm}(\text{CP})_\alpha$  appears. This phase is similar to the  $\text{SmC}_\alpha$  phase of chiral, rod-shaped molecules [?, ?, ?, ?], but with the chirality appearing here as a broken symmetry. A periodic azimuthal precession of the

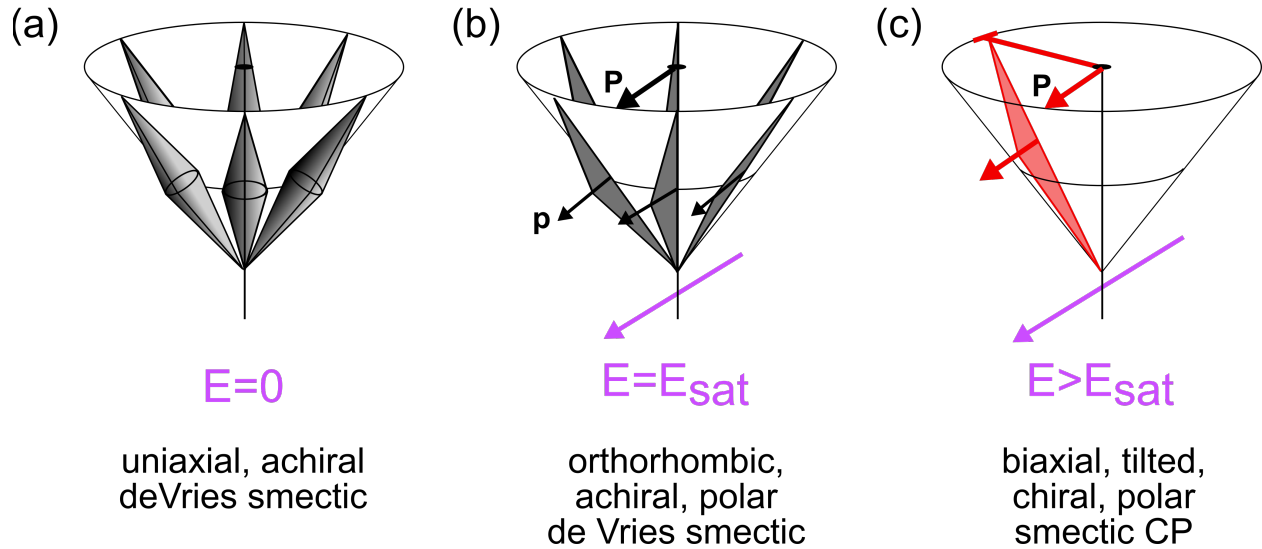


Figure 1.16: Evolution of de Vries SmA bent-core phase under the application of a field

director about the layer normal that is incommensurate with the smectic layering is confirmed by the presence of Bragg reflection peaks in carbon-edge resonant soft X-ray scattering. The absence of the corresponding resonant Umklapp peak unambiguously identifies this structure as a helical modulation of the orientational ordering in which molecules exhibit substantial coupled rotational/positional out-of-layer fluctuations, forming a twist-bend-like helix.